Sensors and Actuators B 255 (2018) 1884–1896

Contents lists available at ScienceDirect

Sensors and Actuators B: Chemical

journal homepage: www.elsevier.com/locate/snb

Sensing behavior to ppm-level gases and synergistic sensing mechanism in metal-functionalized rGO-loaded ZnO nanofibers

Zain Ul Abideen[a], Jae-Hun Kim[a], Ali Mirzaei[b], Hyoun Woo Kim[c,*], Sang Sub Kim[a,*]

[a] Department of Materials Science and Engineering, Inha University, Incheon 22212, Republic of Korea
[b] The Research Institute of Industrial Science, Hanyang University, Seoul 04763, Republic of Korea
[c] Division of Materials Science and Engineering, Hanyang University, Seoul 04763, Republic of Korea

ARTICLE INFO

Article history:
Received 24 April 2017
Received in revised form 12 August 2017
Accepted 30 August 2017
Available online 21 September 2017

Keywords:
ZnO
Metal oxide
Reduced graphene oxide
Pd
Au
Gas sensor

ABSTRACT

Noble metal-functionalized, reduced graphene oxide (rGO)-loaded metal oxides are a new class of ternary composites that combine the advantages of each component, resulting in exceptional materials. But, there are few reports on their use as gas sensors. This paper reports the gas sensing behavior of Au or Pd-functionalized rGO-loaded ZnO nanofibers (NFs) synthesized by using a combination of facile, cost-effective sol-gel and electrospinning methods. An examination of the gas sensing properties revealed that Au-functionalized NFs have a very high response to CO gas. In particular, the gas response (R_a/R_g) to 1ppm of CO was as high as 23.5, whereas Pd-functionalized NFs showed a high response to C_6H_6 gas (11.8 to 1ppmC_6H_6). The presence of rGO/ZnO heterointerfaces, the catalytic effect of Au and Pd nanoparticles (NPs), and the high surface area of NFs were the main factors that contributed to the strong response of the Au or Pd-functionalized rGO-loaded ZnO NFs sensors. These results show that the combination of noble metals, such as Au or Pd NPs, with rGO and ZnO can impart new gas sensing functionality that is potentially useful for CO or C_6H_6 sensing applications, respectively.

© 2017 Elsevier B.V. All rights reserved.

1. Introduction

Graphene has attracted extensive interest due to its fascinating properties. It has a high surface area ($2630 m^2 g^{-1}$) [1,2], good thermal conductivity (5000W/mK [3]), outstanding electron mobility ($200{,}000 cm^2 V^{-1} s^{-1}$ [4])), good stability and high optical transparency [5]. Due to these promising properties, graphene is used in many areas including energy conversion/storage systems, electrocatalysis and electronic devices [6–8]. Schedin et al. [9] reported the first graphene-based gas sensor in 2007. Unfortunately, graphene is not generally produced on a large scale. Furthermore, it has no band gap and functional groups, which are required for gas adsorption. Therefore, reduced graphene oxide (rGO), a form of graphene produced by the reduction of graphene oxide, which contains many functional groups and defects, is preferred for sensing studies. Moreover, rGO can be synthesized easily at a large scale with low costs [10]. rGO has a lower conductivity, more dangling bonds and defects than intrinsic graphene, which is good for adsorption and interactions with target gases [11]. In addition, rGO can be functionalized easily. Therefore, many scientists have shown interest in exploring rGO as a candidate for gas sensors.

Gas sensors based on pure rGO have low sensitivity because the adsorption of gas molecules on rGO is via the weak Van der Waals interaction, resulting in long response and recovery times, which prevent the widespread use of rGO in highly sensitive gas sensing devices [12]. Many attempts have been made to improve the gas sensing properties of rGO-based gas sensors such as functionalization of rGO by introducing different chemical groups or designing novel nanostructures. On the other hand, metal oxides have been explored extensively as gas sensors because of the relatively high sensitivity of their electrical resistance to adsorbates. Combining rGO with metal oxides to form hybrid nanostructures is particularly interesting because of their desirable synergistic interactions. ZnO loaded with rGO has shown special features because ZnO is a good electron donor (*n*-type) and rGO is an excellent electron acceptor (*p*-type) [13,14]. Furthermore, ZnO has also been extensively used for gas sensors because it possesses a number of advantages including high surface activity, low toxicity, and high electron mobility [15,16].

Very recently, we have investigated the role and effect of rGO nanosheets into electrospun ZnO nanofibers [17]. According to the investigation, an optimized amount loading of rGO nanosheets leads to more resistance change of the ZnO nanofibers during

* Corresponding authors.
E-mail addresses: hyounwoo@hanyang.ac.kr (H.W. Kim), sangsub@inha.ac.kr, sangsub99@gmail.com (S.S. Kim).

http://dx.doi.org/10.1016/j.snb.2017.08.210
0925-4005/© 2017 Elsevier B.V. All rights reserved.

adsorption and desorption of gas molecules mainly due to the role of elctron resovoir by rGO nanosheets and other minor effects. On the other hand, we have studied the particular relationship between kind of noble metals and dominantly interacting gas molecucules [18]. In the study [18], the reason for the selective sensing of CO, C_6H_6, and C_7H_8 by, respectively, functionalizing Au, Pd, and Pt NPs on SnO_2 nanowires has been discussed in detail. Accordingly, it is worthy to confirm the synergistic effect of the loading of rGO nanosheets and functionalizing metal NPs to improve the selective gas-sensing capability of ZnO nanofibers.

In our previous study [17], we observed that the resistance and response of the rGO-loaded ZnO NFs sensors increased upon the addition of rGO and reached a maximum value at 0.44wt.%. At higher concentrations of rGO, the resistance of rGO-loaded ZnO decreased, and further addition of rGO had no significant effect on the response of the sensors. Although different optimal amounts of metal functionalization have been reported [19–21] in the literature, in this study 1wt.% of either Au or Pd was chosen because of the promising results of a previous study [22], where 1wt.% Au-functionalized rGO-loaded SnO_2 NFs showed a strong response to reducing gases. In addition, the sensing results were compared with those of rGO-loaded ZnO NFs without functionalization.

In this study, Au or Pd NPs were functionalized on rGO-loaded ZnO NFs composites prepared by an electrospinning process, and the resulting materials were assessed for gas sensing applications. Gas sensing tests at different temperatures and in the presence of different concentrations of target gases were carried out on these unique structures. We found that the Au-functionalized rGO-loaded ZnO NFs can detect concentrations as low as 1ppm of CO gas in the air, and composites functionalized by Pd NPs could easily detect 1ppm of C_6H_6 gas. These new ternary advanced composites can be used for the detection of extremely low concentrations of CO and C_6H_6 gases with good precision.

2. Materials and methods

2.1. Materials

Zinc acetate ($Zn(CH_3CO_2)_2$, (purity >99%), graphene oxide (GO), N, N-dimethyl formamide (DMF) and polyvinyl alcohol (PVA, MW 80,000) were purchased from Sigma-Aldrich. Hydrazine monohydrate (N_2H_4. H_2O), $PdCl_2$, acetone, 2-propanol and hydrogen tetrachloroaurate (III) hydrate ($HAuCl_4{\cdot}3.5H_2O$) were obtained from Kojima Chemical. Ethanol, methanol, isopropanol, and deionized (DI) water were used for washing and solvent preparation. All starting materials were used without additional purification.

2.2. Preparation of rGO

Graphene oxide (GO) was synthesized from graphite powder using a modified Hummers and Offeman method [23]. To reduce GO, 10mL of hydrazine monohydrate was added to the GO suspension, and the mixture was heated at 150°C for 24h. The products were then isolated by centrifugation at 12,000rpm for 45min, and were washed with DI water and methanol until the pH of the solution reached 7 to afford pure rGO powder. The preparation process of the rGO solution is described in detail elsewhere [24].

2.3. Synthesis of Au/Pd-functionalized rGO/ZnO composite NFs

2.3.1. Preparation of electrospinning solutions

Sol-gel and electrospinning methods were used for the synthesis of Au or Pd-functionalized rGO-loaded ZnO composite NFs. First, an aqueous solution of PVA was prepared by dissolving PVA in DI water with constant stirring for 4h. Subsequently, 1g $Zn(CH_3CO_2)_2$ was added to the prepared PVA solution and the mixture was stirred for 10h. An aqueous solution of $HAuCl_4{\cdot}nH_2O$ was prepared separately by mixing 0.0007g of $HAuCl_4{\cdot}nH_2O$ with isopropanol followed by constant stirring for 1h. $PdCl_2$ was dissolved in a mixed solution of acetone (50 vol.%) and 2-propanol (50 vol.%) for the preparation of Pd NPs. The prepared Au and Pd precursor solutions were then exposed to UV radiation for 1min. This led to the growth of Au and Pd NPs in their respective solutions. In a separate beaker, rGO was mixed with DI water to prepare an rGO suspension. Then, the rGO suspension was separately added into both Au and Pd solutions. The prepared Au/rGO and Pd/rGO suspensions were then mixed into PVA/Zn $(CH_3CO_2)_2$ solutions separately. Vigorous stirring for 1h eventually resulted in the formation of two viscous solutions of PVA/Zn $(CH_3CO_2)_2$ containing Au NPs or Pd NPs and rGO (0.44wt.%).

2.3.2. Electrospinning process

The prepared precursor solution was loaded into a syringe with a 21-gauge needle (inner diameter of 0.51mm). The composite fibers were electrospun by applying a 15kV bias using a power supply with a distance of 20cm between the tip of the needle and a ground plate. The feeding rate of the solution was adjusted accurately to a constant value of 0.03mL/h. The electrospun NFs were obtained over the SiO_2-grown Si wafers that had been placed on the metal collector. All electrospinning experiments were carried out at room temperature. The as-spun NFs were subsequently calcined at a temperature of 600°C for 30min in air at a heating rate of 2°C/min. The synthesis procedure for the NFs by electrospinning is described in detail elsewhere [25]. A similar method was used to prepare the Pd-functionalized rGO-loaded ZnO composite NFs. The amount of rGO was ~0.44%wt according to a previous study [17] and the amount of Pd and Au NPs was set to be~1%wt.

2.4. Sensing measurements

To examine the sensing behavior of Au or Pd-functionalized rGO-loaded ZnO NFs, double layer electrodes consisting of Ti (thickness ~50nm) and Pt (thickness ~200nm) were deposited sequentially onto the specimens by radio frequency magnetron sputtering at room temperature. Subsequently, the gas sensing properties of the composite sensors towards various reducing gases (CO, C_6H_6 and C_7H_8) at concentrations ranging from 1 to 5ppm were measured under atmospheric pressure at operating temperatures between 300 and 450°C. The measurements were conducted using a gas dilution and sensing system. The sensors were placed and evaluated in the testing chamber at constant temperatures, and the operating temperature of the sensors was controlled by an external heating source. More details related to the sensor design, gas dilution, and the sensing system are provided in our earlier reports [24,26]. The sensors were stabilized for ~20min in the baseline gas (synthetic dry air) to obtain a stable resistance at every operating temperature (prior to the gas sensing tests). The gas concentration was controlled precisely by changing the mixing ratio of the dry air-balanced target gas and the synthetic dry air through accurate mass flow controllers. The response of the sensors to the reducing gas is defined as the ratio of R_a to R_g. Here, R_a is the original base resistance of the sensor in air, and R_g is the stabilized resistance of the sensor in the presence of the applied gas. The response time (τ_{res}) is defined as the time in which the resistance of the sensor changes to 90% of the original base resistance, and the recovery time (τ_{rec}) is defined as the time needed until 90% of the signal is recovered. Fig. 1 schematically shows the main steps to synthesize the Au or Pd-functionalized rGO-loaded ZnO NFs.

2.5. Characterization

The microstructure and phase composition of the synthesized Au or Pd-functionalized rGO-loaded ZnO composite NFs were

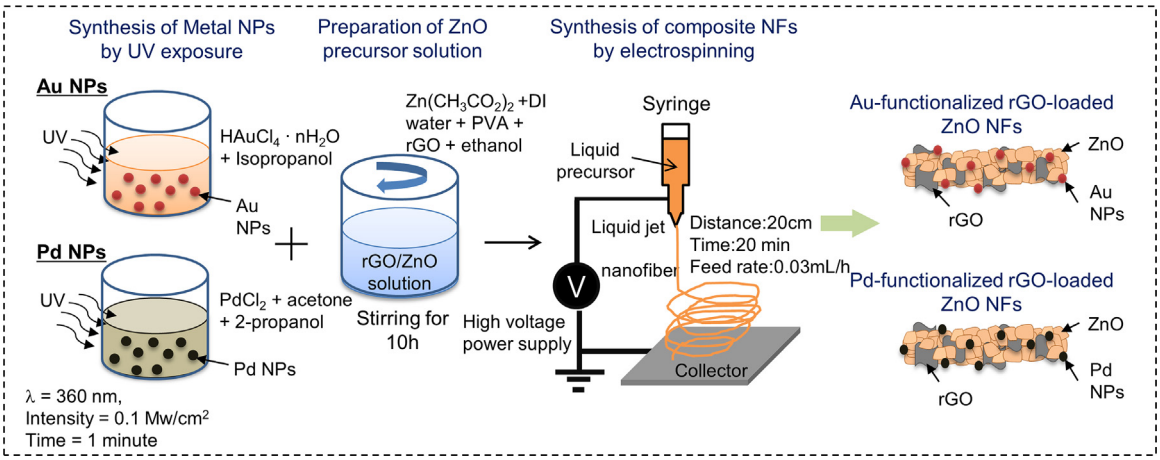

Fig. 1. Schematic illustration of the synthesis procedure for Au- or Pd-functionalized rGO-loaded ZnO NFs.

investigated by field-emission scanning electron microscopy (FE-SEM, Hitachi S-4200) and high-resolution transmission electron microscopy (HR-TEM, Phillips CM-200). Energy-dispersive X-ray spectroscopy (EDXS) was performed in conjunction with TEM. The chemical composition of surfaces was analyzed by X-ray Photoelectron Spectroscopy (XPS) using a commercial instrument (XPS, Thermo K-Alpha) operating with an Mg Kα X-ray source. The binding energy scale of the XPS spectra was calibrated by setting the peak energy of adventitious carbon (C 1s peak) to 285 eV.

3. Results and discussion

3.1. Structure, morphology and composition analyses

Figs. 2(a) and (b) show XRD patterns of Au- and Pd-functionalized rGO-loaded ZnO NFs, where all the peaks shown as hollow circles can be attributed to crystalline planes of ZnO (JCPDS Card No. 89-1397). The high intensity of the peaks demonstrates the high crystallinity of ZnO. In addition, four peaks shown as hollow orange squares belong to Au with a face-centered cubic structure (JCPDS Card No. 89-3697), and one peak shown as a hollow green square belongs to Pd having a face-centered cubic structure (JCPDS Card No. 87-0641). No other phase or impurity can be observed in the XRD patterns, which indicates the high purity of the synthesized NFs and demonstrates the success of the synthesis procedure.

The results of TEM analyses are shown in Fig. 3. A representative TEM image of Au-functionalized rGO-loaded ZnO NFs is shown in Fig. 3(a), where a transparent rGO sheet is observed. Fig. 3(b) shows ZnO nanograins within a single ZnO NF. As shown, ZnO nanograins with an approximate diameter of 20–25nm were observed. Fig. 3(c) shows a lattice-resolved TEM image, where fringes with a spacing of 0.236nm can be attributed to the (111) plane of Au. Fig. 3(d-1)-(d-4) show EDAX color maps of Au-functionalized rGO-loaded ZnO NFs taken from Fig. 3(d). Zn, O, C, and Au elements exist in the NFs. Also, Fig. 3(e) presents an EDAX analysis, where the presence of Au, Zn, O, and C peaks demonstrate the co-existence of Au, rGO and ZnO in the synthesized NFs.

A typical TEM image of a Pd-functionalized rGO-loaded ZnO NF is presented in Fig. 3(f). ZnO nanograins formed the NF, which had an approximate diameter of 200nm. The lattice-resolved TEM image is presented in Fig. 3(g), where the spacings between parallel fringes of 0.25nm and 0.22nm can be indexed to the (101) and (111) planes of ZnO and Pd, respectively. Figs. 3(h-1)-(h-4) show EDAX color maps taken from Fig. 3(h). Zn, O, C and Pd elements were observed, confirming their existence in the NFs.

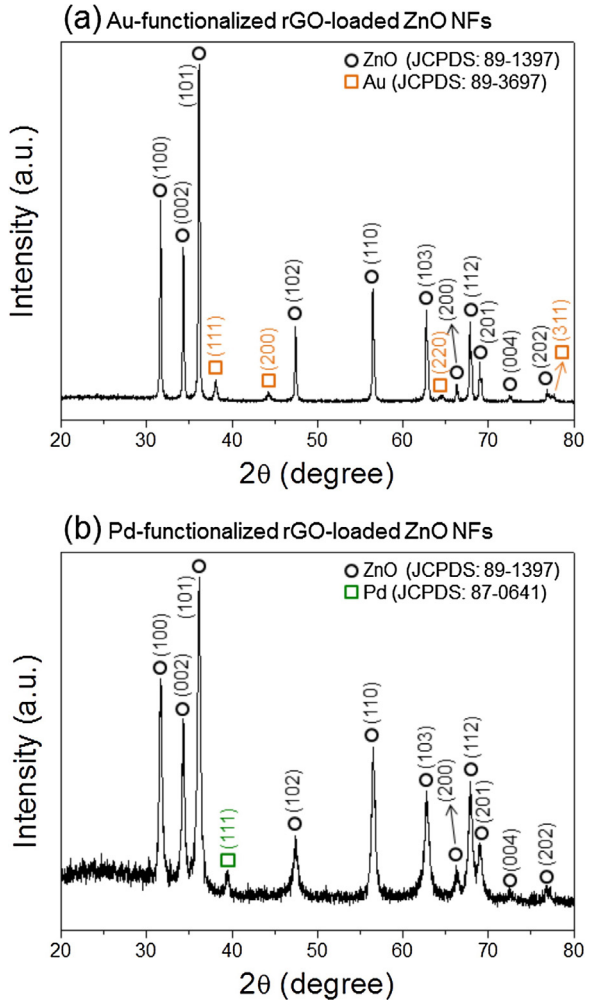

Fig. 2. XRD patterns of (a) Au- and (b) Pd-functionalized rGO-loaded ZnO NFs, respectively.

TEM and EDAX results showed that ZnO was the main component of the ternary composite and that it was in the form of a one-dimensional NF. Even though the Pd or Au NPs were not completely localized at the surfaces of ZnO NFs, we assumed that Pd and Au NPs were mainly distributed on the surface of ZnO NFs as isolated islands due to the very small diameter of the NFs and the observed enhanced sensing behavior of the sensors. In addi-

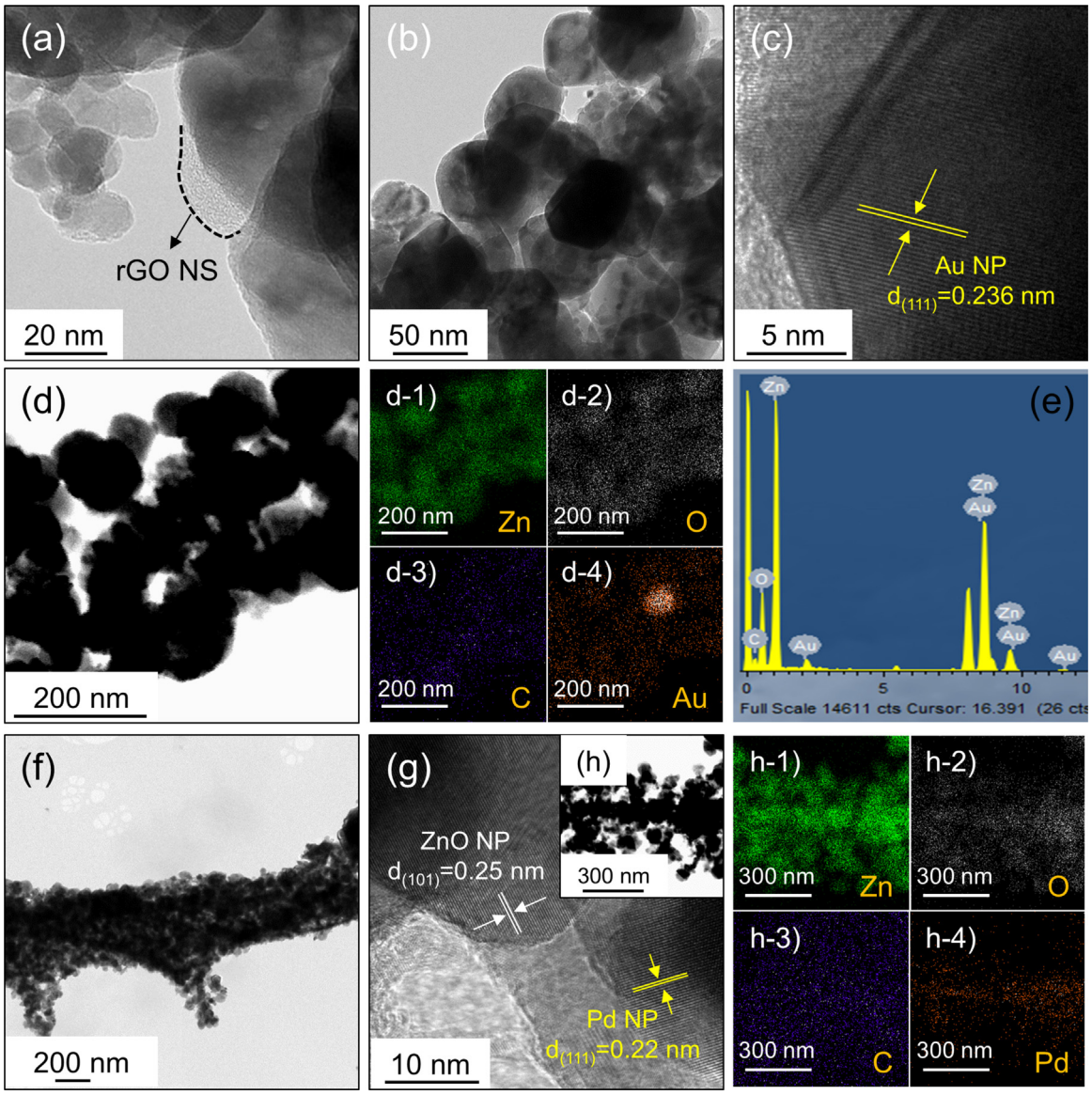

Fig. 3. (a) TEM image of Au-functionalized rGO-loaded ZnO NF. (b) TEM image of a ZnO NF. (c) Lattice-resolved TEM image of Au-functionalized rGO-loaded ZnO NF. (d) TEM image of Au-functionalized rGO-loaded ZnO NF with corresponding EDAX color maps of (d-1) Zn (d-2) O, (d-3) C, and (d-4) Au elements. (f) TEM image of Pd-functionalized rGO-loaded ZnO NF. (g) Lattice-resolved TEM image of Pd-functionalized rGO-loaded ZnO NF. (h) TEM image of Pd-functionalized rGO-loaded ZnO NF with corresponding EDAX color maps of (h-1) Zn (h-2) O, (h-3) C and (h-4) Pd elements.

tion, rGOs with ultrathin nanosheet morphologies were mainly distributed on the surfaces of ZnO NFs.

XPS analysis was used to further evaluate the purity and the composition of the synthesized NFs. Fig. 4(a) shows an XPS spectrum of Pd-functionalized rGO-loaded ZnO NFs. Only peaks of expected elements were observed, and no impurities were found in the synthesized products. Fig. 4(b) presents the Zn 2p core level region, which is split into a Zn $2p_{3/2}$ peak at a lower binding energy of 1022.08eV and a Zn $2p_{1/2}$ peak at 1045.18eV [27]. The spin-orbit splitting of ~23eV for Zn $2p_{3/2}$ and Zn $2p_{1/2}$ confirms the complete oxidization of Zn atoms [28]. A high-resolution spectrum of the Pd 3d core level is presented in Fig. 4(c). The peaks located at 337.08eV and 342.58eV have a separation of approximately 5.5 eV, which agrees with the spin-orbit doublet separation value attributed to the formation of PdO [29]. According to the XPS and HRTEM results, we concluded that both metallic Pd NPs and PdO exist in the synthesized NFs. Figs. 4(d) and (e) show spectra of C1s (285.68eV) and O1s core level regions, respectively. The high intense peak located at 530.88eV belongs to the crystal lattice oxygen ions (O_{latt}) in the form of ZnO [27].

Fig. 5(a) shows an XPS spectrum of Au-functionalized rGO-loaded ZnO NFs, and no undesirable element was observed. Fig. 5(b) shows the high-resolution region of the Zn 2p core level. Similar to Fig. 4(b), Zn has a doublet corresponding to Zn $2p_{3/2}$ at 1022.00eV and Zn $2p_{1/2}$ at 1045.08eV and has a+2 oxidation state. The Au 4f core level region is shown in Fig. 5(c). As shown, the Au chemical state has two separate peaks located at 83.88 and 88.98 eV, which are due to the Au $4f_{7/2}$ and Au $4f_{5/2}$ transitions of metallic Au, respectively [30]. The presence of an overlapping shoulder was observed at 91.98 eV; this is assigned to Zn 3p and confirms the co-existence of Au and ZnO [30]. Peaks related to the oxidized form of Au located around 85.5 and 86.3eV were not detected [31]. Figs. 5(d) and (e) also show the spectra of C 1s (285.68eV) and O 1s (530.88) core level regions, respectively.

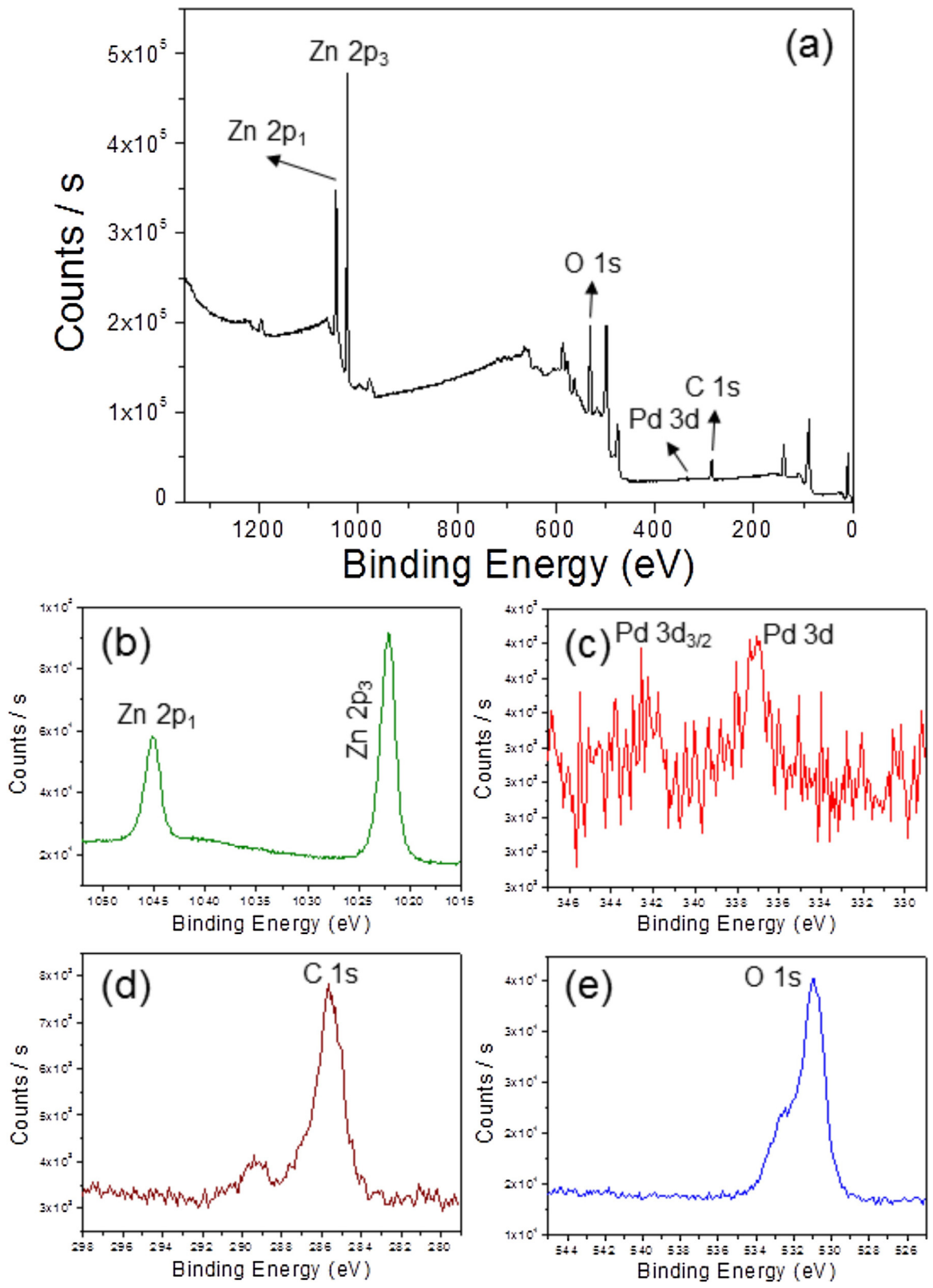

Fig. 4. (a) XPS spectrum of Pd-functionalized rGO-loaded ZnO NFs, (b) Zn 2p core level region, (c) Pd 3d core level region, (d) C 1s core level region, and (e) O 1s core level region.

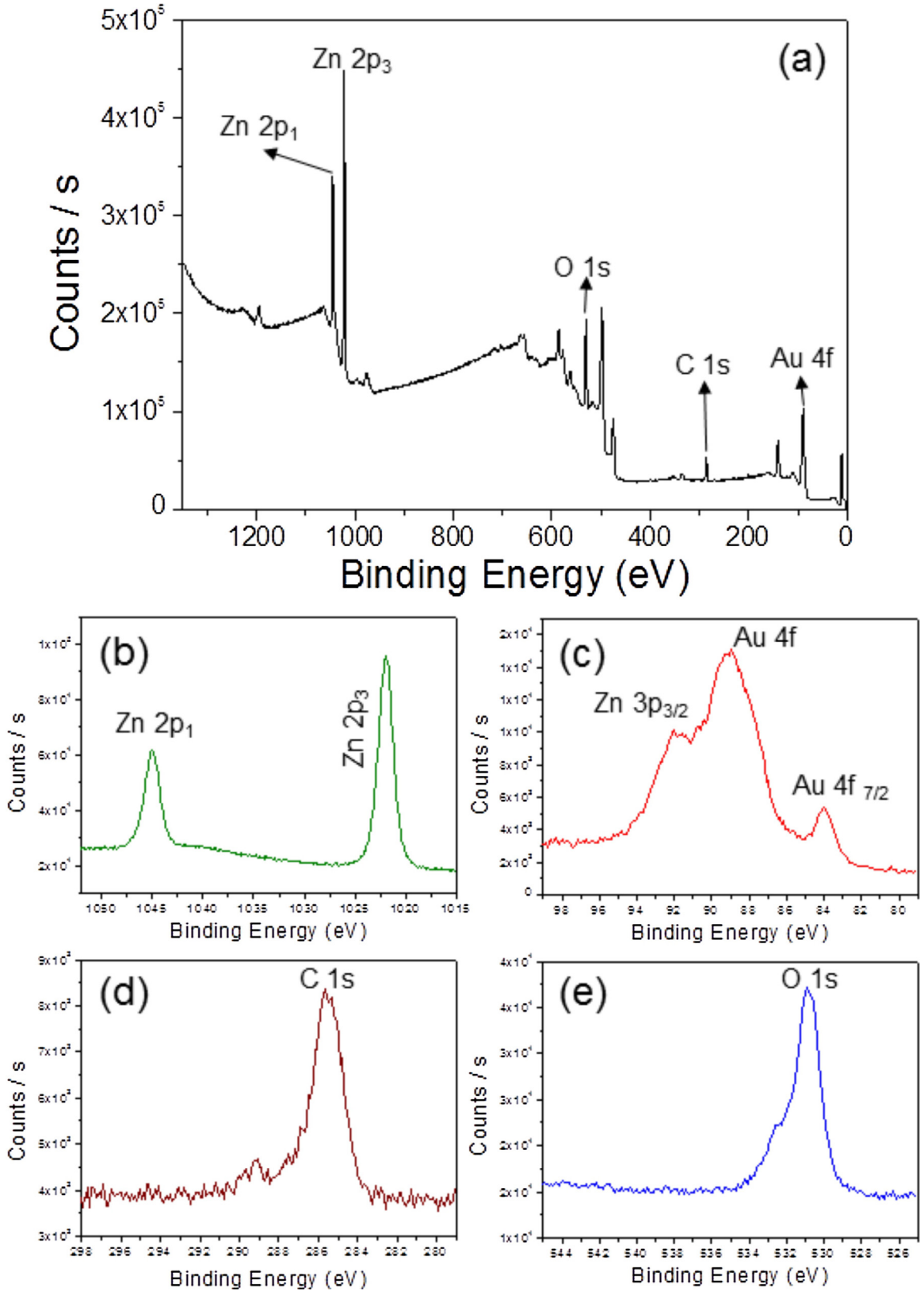

Fig. 5. (a) XPS spectrum of Au-functionalized rGO-loaded ZnO NFs, (b) Zn 2p core level region, (c) Au 4d core level region, (d) C 1s core level region, and (e) O 1s core level region.

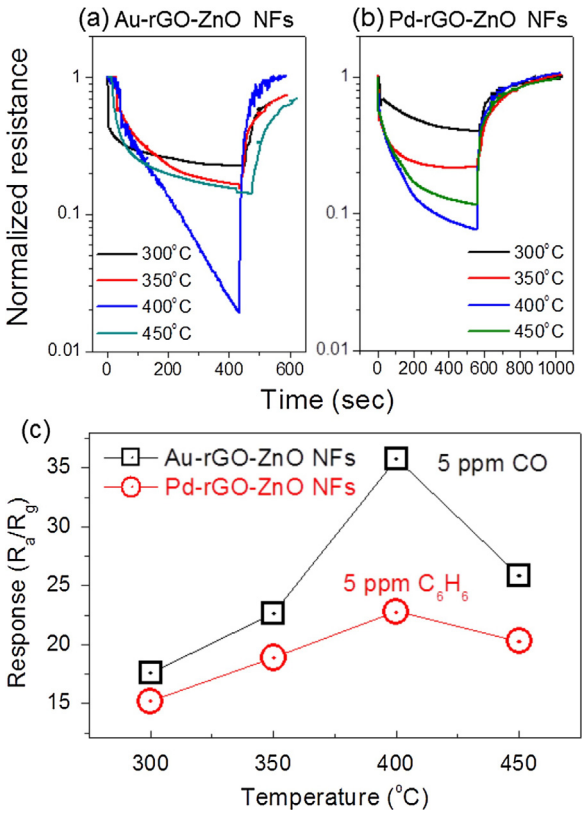

Fig. 6. **(a)** Dynamic normalized resistances of the Au-functionalized rGO-loaded ZnO NFs sensor to 5ppm CO gas at different temperatures. (b) Dynamic normalized resistances of the Pd-functionalized rGO-loaded ZnO NFs sensor to 5ppmC_6H_6 gas at different temperatures. (c) Temperature dependence of the response of the Au-functionalized rGO-loaded ZnO NF sensor and the Pd-functionalized rGO-loaded ZnO NFs sensor to CO and C_6H_6 gases.

3.2. Gas sensing studies

It is well-known that the working temperature has a significant effect on the sensing behavior. Several factors such as oxygen species, rates of adsorption and desorption, the charge-carrier concentration and the Debye length, depend greatly on the sensor operating temperature. The Debye length for a metal oxide can be calculated as follows [32–34]:

$$\text{DebyeLength}(\lambda) = \sqrt{\frac{\varepsilon kT}{q^2 n_c}} \quad (1)$$

Here, λ depends on ε (the dielectric constant), k (Boltzmann's constant), T (the absolute temperature) and the n_c (the carrier charge concentration) of material. In the above equation, "q" is the charge of an electron (1.6×10^{-19}C).

In other words, gas sensors have higher sensitivities when large numbers of active electrons participate in the reaction at the optimal temperature [35]. To determine the optimal operating temperature, the sensors were exposed to a fixed 5ppm CO and 5ppmC_6H_6 gas concentration at different temperatures. Fig. 6 (a) and (b) show the transient responses of the Au-functionalized rGO-loaded ZnO NFs to 5ppm CO gas and the Pd-functionalized rGO-loaded ZnO NFs to 5ppmC_6H_6 gas at different temperatures from 300 to 450°C, respectively. Fig. 6(c) shows variations in the responses of the two sensors for various operating temperatures. For both sensors, the response increases with increasing operating temperature, reaching a maximum sensitivity at 400°C. The response decreased thereafter with a further increase in the operating temperature. Therefore, 400°C is regarded as the optimal operating temperature of the sensors. The maximum response to 5ppm CO gas was 35.8 for the Au-functionalized rGO-loaded ZnO NFs sensor and 23 for 5ppmC_6H_6 in the case of the Pd-functionalized rGO-loaded ZnO NFs sensor. The temperature dependence of the response to the reducing gas [R] is determined by the following processes: (i) dissociative adsorption of oxygen (molecular oxygen does not interact with reducing gas), (ii) adsorption of [R] molecules, (iii) desorption of [R], and (iv) desorption of chemisorbed oxygen. The first two processes determine the drop in response at low operating temperatures, and the last two processes determine the decrease in response at high temperatures. In general, a competition among these processes is believed to determine the operating temperature of the maximum response [36]. The increase in response with operating temperature (forT_{op} <400°C) may be because there is enough thermal energy to overcome the reaction activation energy barrier, resulting in a significant increase in electron concentration from the sensing reaction. The decrease in response above 400°C could be due to a reduction in exothermic CO gas adsorption [37].

At the optimal operating temperature (400°C), the response of both sensors at 1, 2, and 5ppm of CO, C_6H_6 and C_7H_8 gases was investigated. Fig. 7(a) shows the dynamic response of the Au-functionalized rGO-loaded ZnO NFs sensor to 1, 2 and 5ppm CO gas at 400°C, and Fig. 7(b) presents the corresponding calibration curves. The reversible cycles of the response curves indicate that the responses of the gas sensors are stable and repeatable. Upon exposure to reducing gases, the sensor resistance decreased initially due to the release of free electrons, and then became saturated. When the gas supply was stopped, the resistance increased and nearly returned to its baseline value, showing *n*-type behavior of the sensor due to the *n*-type features of ZnO, which is the main component of the sensor. The calibration curves show that the responses of the sensor to 1, 2, and 5ppm CO gas were 23.5, 29.6, and 35.8, respectively. Under the same conditions, the responses to C_6H_6 and C_7H_8 gases were 17.6, 26.4 and 29.1, and 15.0, 18.2 and 21.0, respectively. The order of the response to gases at any concentration is as follows: $R_{CO}>R_{C6H6}>R_{C7H8}$. Fig. 7(c) shows the dynamic responses of the Pd-functionalized rGO-loaded ZnO NFs at 400°C to 1, 2, and 5ppm CO, C_6H_6 and C_7H_8 gases, and Fig. 7(d) presents the corresponding calibration curves. According to the calibration curves, the responses of the sensor to 1, 2 and 5ppm CO gas were 8.6, 11.9 and 13.8, respectively, and the responses to 1, 2 and 5ppmC_6H_6 gas were 11.8, 17.1, and 23.0 respectively. The responses to 1, 2 and 5ppmC_7H_8 gas were 11.5, 16.7 and 20.5, respectively. Therefore, this sensor shows the highest response to C_6H_6 gas and the lowest response to CO gas.

The relationship between the sensor response ($S=R_a/R_g$) and gas concentration (C_{gas}) can be expressed according to the following power law [38]:

$$S = (1 + k[C_{gas}]^{\beta}) \quad (2)$$

where k, β and [C_{gas}] are a constant, a power-law exponent and the gas concentration (ppm), respectively. According to the above equation, the response is proportional to the gas concentration. Fig. 8 shows a logarithmic plot of the sensing data. Plots of ln(S-1) versus ln(C) for both sensors give straight lines, which can be expressed as ln(S-1)=3.13+0.268 ln(C_{CO}) for the Au-functionalized rGO-loaded ZnO NF sensor and ln(S-1)=2.41+0.43 ln(C_{C6H6}) for the Pd-functionalized rGO-loaded ZnO NF sensor. These relationships can be used to estimate the concentration of CO or C_6H_6 based on the change in the response of the sensor.

The response times/recovery times of the Au-functionalized sensors to 5ppm CO and C_6H_6 gases were 177.3/76.1s and 191.3/82.1s, respectively, and those of the Pd-functionalized sensors were 103.8/320.7s and 110.3/318.2, respectively, as shown

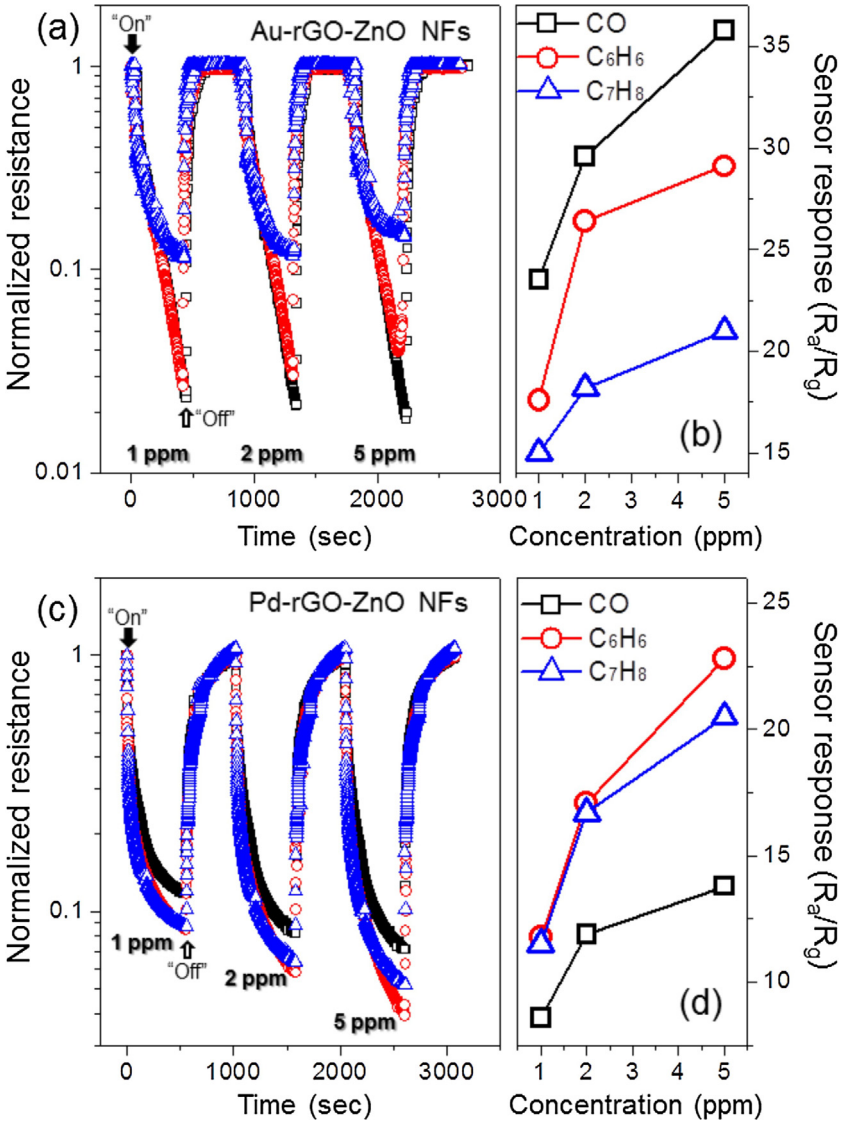

Fig. 7. **(a)** Dynamic normalized resistances of the Au-functionalized rGO-loaded ZnO NFs sensor to different concentrations of CO, C_6H_6 and C_7H_8 gases. (b) Corresponding calibration curves. (c) Dynamic normalized resistances of the Pd-functionalized rGO-loaded ZnO NFs sensor to different concentrations of CO, C_6H_6 and C_7H_8 gases. (d) Corresponding calibration curves.

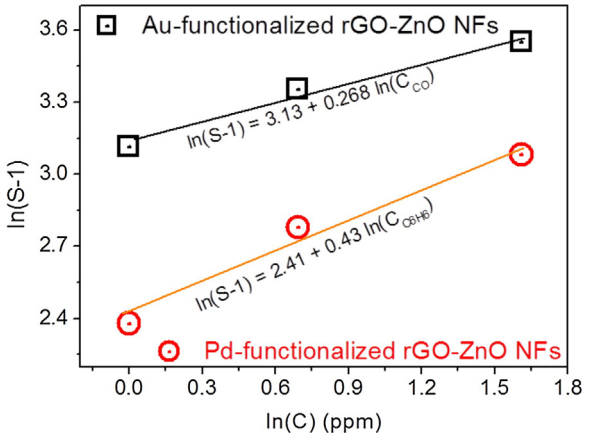

Fig. 8. ln (S-1) versus ln (gas concentration) for the Au-functionalized rGO-loaded ZnO NFs and the Pd-functionalized rGO-loaded ZnO NFs.

in Fig. 9. At such low concentrations, the response times were relatively short. For both gases, the response times for the Pd-functionalized sensors were shorter than the recovery times, whereas the recovery process for the Au-functionalized sensors were faster than the response process. Three factors govern the response and recovery times of the sensors: temperature, energy of adsorption/desorption and sensor morphology. The temperature is same for both sensors, meaning that this factor can be excluded. The morphology of the fibrous structure does not change due to the functionalization with Au or Pd NPs. Therefore, the morphology factor can also be ignored in the analysis. Therefore, the results suggest that the adsorption energy of both gases for the Pd-functionalized NFs is lower than the desorption energy, whereas the reverse is true for the Au-functionalized composite NFs.

Fig. 10 compares the responses of the Au-functionalized rGO-loaded ZnO NFs sensor, Pd-functionalized rGO-loaded ZnO NFs sensor, the rGO-loaded ZnO NFs sensor and pristine ZnO NF sensor for 5ppm CO and C_6H_6 gases at 400°C. The results of the rGO-loaded ZnO NFs and pristine ZnO NFs were taken from the authors' previous study [17]. The responses of Au-functionalized rGO-loaded ZnO NF, Pd-functionalized rGO-loaded ZnO NF, rGO-loaded ZnO NF

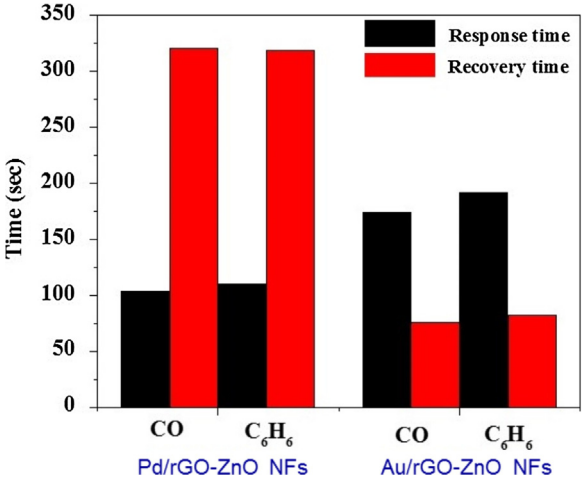

Fig. 9. Response and recovery times for Au- and Pd- functionalized rGO-loaded ZnO NF sensors.

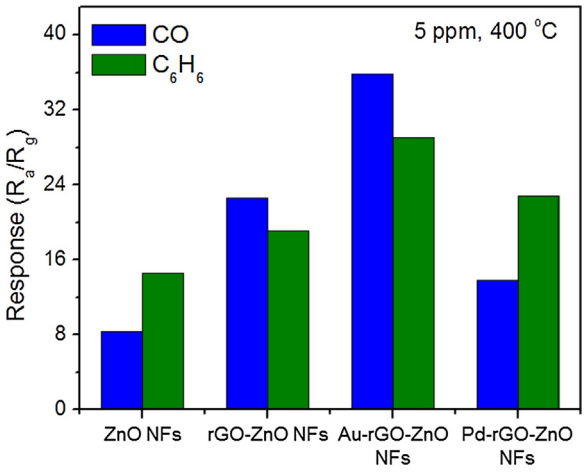

Fig. 10. Comparison of responses of different sensors to 5ppm CO and C_6H_6 gases at 400°C.

and pristine ZnO NF sensors to 5ppm CO gas were 35.8, 13.8, 22.6, and 8.4, and the responses to C_6H_6 gas were 29.1, 22.8, 19.1, and 14.6, respectively. This demonstrates the favorable effects of Au and Pd functionalization for detection of CO and C_6H_6 gas, respectively. The main reasons for the high response of Au- or Pd- functionalized rGO-loaded ZnO NF sensors to CO and C_6H_6 gases will be discussed in the next section.

3.3. Gas sensing mechanism

The interaction of gaseous species with semiconductor-based sensors includes two steps. First, molecular oxygen in the atmosphere reacts with the sensor. Due to its high electronegativity, oxygen gas is chemisorbed on the surface of the sensor in the forms of O_2^-, O^- and O^{-2} depending on the operating temperature (T_{op}) of the sensor [39]:

$$O_2\,(gas) \rightarrow O_2\,(ads) \tag{3}$$

$$O_2\,(ads) + e^- \rightarrow O_2^-\,(ads) \quad (T_{op} < 100^\circ C) \tag{4}$$

$$O_2^- + e^- \rightarrow 2O^- \quad (100 < T_{op} < 300^\circ C) \tag{5}$$

$$O^- + e^- \rightarrow O^{2-} \quad (T_{op} > 300^\circ C) \tag{6}$$

These reactions produce oxygen adsorbates and deplete electrons from the conduction band of the semiconducting metal oxide. The second step involves the reaction of the target gases with the adsorbed oxygen species. For CO and C_6H_6 gases, the relevant reactions can be expressed as follows:

$$2CO + O_2^-(ads) \rightarrow 2CO_2 + e^-$$
$$C_6H_6 + \frac{15}{2}O_2^- \rightarrow 6CO_2 + 3H_2O + 15e^- \quad (T_{op} < 100^\circ C) \tag{7}$$

$$O + O^- \rightarrow CO_2 + e^-$$
$$C_6H_6 + 13O^- \rightarrow 6CO_2 + 3H_2O + 13e^- \quad (100 < T_{op} < 300^\circ C) \tag{8}$$

$$CO + O^{2-} \rightarrow CO_2 + 2e^-$$
$$C_6H_6 + 13O^{2-} \rightarrow 6CO_2 + 3H_2O + 26e^- \quad (T_{op} > 300^\circ C) \tag{9}$$

Therefore, electrons are released and the conductivity increases, causing the response in the sensor.

Several factors must be considered to explain the sensing mechanisms in the Au- or Pd-functionalized rGO-loaded ZnO NFs. First, there is a change in the resistance along the surface of the individual ZnO NFs. According to Eqs. (3)–(6), oxygen molecules in air will be adsorbed on the surface of ZnO. An electron-depleted region is then established below the surface due to the extraction of electrons by these adsorbed oxygen ions. The width of the depleted region decreases as the chemisorbed oxygen reacts with reducing gases, such as CO or C_6H_6 gas (Eqs. (7)–(9)). Consequently, this change in the depletion layer width will result in a response.

Second, the gas sensing properties of NFs are also related to the presence of nanograins. The polycrystalline ZnO NFs have many ZnO/ZnO homointerfaces. The boundaries between these nanograins act as potential barriers to the flow of electrons. When reducing gases are introduced, the heights of these potential barriers will become lower, thereby decreasing the resistance across the grain boundaries through the ZnO NF, which contributes to the gas response.

Third, many rGO-loaded ZnO heterojunctions can exist on the rGO-loaded ZnO NFs, which are effective in enhancing the response of the sensor. ZnO is an *n*-type metal oxide, whereas rGO has *p*-type semiconducting properties. Therefore, at the interfaces of rGO/ZnO, electrons flow from ZnO to rGO to establish the equilibrium *p-n* heterointerface. This indicates that the embedded rGO acts as an electron acceptor, resulting in an expansion of the depletion layer of ZnO NFs. When reducing gases interact with pre-adsorbed oxygen species on the surfaces of NFs, more variation in the already-expanded depletion layer is expected, which is the source of the enhanced sensing response observed in rGO-loaded ZnO NFs.

Fourth, rGO possesses a very high surface area, which can provide plenty of adsorption sites for target gases, resulting in enhanced gas response [40]. Also, defects and functional groups on the rGO surface can provide additional adsorption sites for the gas molecules, consequently increasing the gas response. However, rGO has some residual oxygen species that are sp^3 bonded to the carbon atoms, just like GO. These groups are not active in the gas adsorption process, and the high temperature heating of rGO may reduce the amount of these oxygen species [17]. Further reduction of the rGO sheets may take place by the loss of oxygen upon heating at 400°C during the sensing tests. As a result, the reduced surface can provide adsorption sites for the target gas, and therefore the response can be enhanced by the loss of sp^3 bonded oxygen species.

Fifth, the role of metal NPs must be considered. Generally, two different mechanisms, namely electronic sensitization (ES) and chemical sensitization (CS), describe the promotional role of noble metals on the gas sensing [41]. In the case of ES, which is observed for Pd/PdO, the PdO NPs on the surface of ZnO NFs act as strong acceptors of electrons from the ZnO. This results in depletion of electrons near the interface. When the PdO NPs are reduced in the

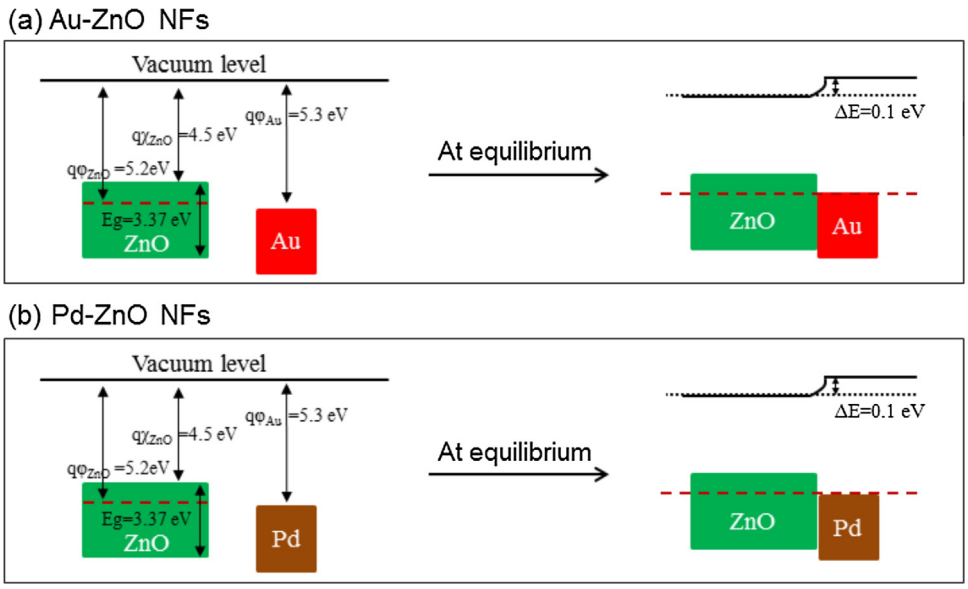

Fig. 11. Band structure of (a) Au-ZnO and (b) Pd-ZnO.

presence of target gases such as CO or C_6H_6, the space charge layer is relaxed by releasing back electrons to the ZnO. This change in the oxidation state of Pd is responsible for the enhanced gas response. However, this sensitization does not occur for Au NPs because they are not oxidized easily in air [42]. In CS, Au and Pd NPs increase the adsorption of oxygen molecules due to the spillover effect. They will generate more oxygen species and more reactive sites on the ZnO surface compared to pristine ZnO. This chemical mechanism will result in more trapped electrons, and consequently, the electron depletion layer will be thicker [43,44]. This mechanism is effective for both Au and Pd NPs, which eventually enhances the gas response of the sensor.

Sixth, the introduction of metal catalysts inevitably generates metal-ZnO and metal-rGO heterointerfaces. In the present system, the work functions of Au (~5.3eV [45]) and Pd (~5.3eV [18]) are larger than those of ZnO (5.2eV [17]) and rGO (4.75eV [17]). In the heterointerferances between Pd/ZnO and Au/ZnO, electrons will flow from ZnO to Pd and Au NPs to align the Fermi levels, and nano-Schottky barriers will be formed, as shown in Fig. 11. As a result, the width of the electron depletion layer in ZnO NFs will expand, in sharp contrast to the case of pristine ZnO. After exposure to reducing gases such as CO and C_6H_6, the width of the depletion layer will be greatly reduced due to the release of electrons from the reactions between reducing gas and adsorbed oxygen species. This eventually leads to a greater increase in response relative to pristine ZnO NFs.

The electron pathways in the ternary composite are also important. ZnO is the main component in the ternary composite, and the amounts of Au or Pd NPs (1wt%) and rGO (0.44wt%) are much lower. Thus, they are present in the form of isolated entities, and the dominant electrical transport pathway must be localized in the conduction path of ZnO NFs. However, the rGO nanosheets and metal NPs both affect the conduction path due the charge carrier transfer between ZnO and rGO nanosheets or metal NPs, as discussed above.

Table 1
Gas sensing properties of some recently developed rGO-based gas sensors in the literature.

Material	Gas	Conc. (ppm)	Temp (°C)	Response (R_a/R_g)	Ref.
Au/rGO loaded ZnO	CO	5	400	35.8	Present Work
Pd/rGO loaded ZnO	C_6H_6	5	400	22.8	Present Work
Ag/ZnO/Gr	C_2H_2	100	150	21.2 (R_a/R_g)	[37]
Pd/SnO_2/rGO	NH_3	5	25	7.6%(ΔR)/R_a	[57]
Pd/WO_3/rGO	H_2	N/A	100	150(ΔG)/G_a	[58]
ZnO/rGO	HCHO	300	25	45%(ΔR)/R_a	[59]
Co_3O_4 NFs/rGO	NH_3	50	25	53.6%(ΔR)/R_a	[60]
MoO_3/rGO	H_2S	50	160	4120%(ΔR)/R_a	[61]
WO_3 decorated MWCNT/rGO	NO_2	5	200	17(ΔR)/R_a	[62]
Pristine rGO	NO_2	25	25	0.012 (ΔR)/R_a	[63]
TiO_2/N-rGO	Acetone	300	300	14 (I_g/I_a)	[64]
ZnO/rGO	NO_2	2	RT	25.6% (ΔR)/R_a	[12]
Cu_2O NWs/rGO	NO_2	2	RT	267.8%(ΔR)/R_a	[65]
WO_3 NRs/rGO	NO_2	1	300	61%(ΔR)/R_a	[66]
WO_3/rGO	NO_2	5	250	133%(ΔR)/R_a	[67]
NiO/rGO	NO_2	5	200	4.7%(ΔR)/R_a	[68]
Co_3O_4/rGO	NO_2	60	25	80%(ΔR)/R_a	[69]
WO_3/rGO	NO_2	5	25	769%(ΔR)/R_a	[70]
WO_3 NRs/rGO	NO_2	20	300	202%(ΔR)/R_a	[71]
$GdInO_3$/rGO	CO	20	90	48%(ΔR)/R_a	[72]
SnO_2/rGO	NO_2	5	50	3.31 (R_a/R_g)	[73]
SnO_2/rGO	NO_2	100	45	1.038(R_a/R_g)	[74]
SnO_2/rGO	NO_2	0.1	150	10.64%(ΔR)/R_a	[75]
SnO_2/rGO	NO_2	1	75	696%(ΔR)/R_a	[11]

The reason for the favorable effect of Au and Pd functionalization for detection of CO and C_6H_6 gas, respectively, may be as follows. Au NPs are known to be highly efficient CO oxidation catalysts when they are well dispersed and deposited on metal oxide semiconductors [46–50]. The strong response and good selectivity of CO gas in the presence of Au NPs can be attributed to [41] the low oxidation barrier for the oxidation of CO (1.20eV) in the presence of Au. The interaction between CO and Au NPs is very complex, and it depends strongly on the overlap of the 5σ and $2\pi^*$ orbitals of CO with the d orbitals of the Au NP. In fact, CO donates electrons from its σ orbitals to the d_σ orbitals of Au, and the filled d_π orbitals of Au donate electrons back into the empty π orbitals of CO [51].

The Au NPs do not show good performance for C_6H_6 due to the poor adsorption of C_6H_6 on Au at high temperatures. In fact, due to the weak bonding between Au and C, the interaction between C_6H_6 and Au is extremely weak and results only in an increase in the Fermi energy [52]. In addition, good C_6H_6 oxidation by Pd NPs has been reported in the literature [18,53]. It is reported [54] that the good adsorption of C_6H_6 onto Pd can be explained by considering the interaction energies between the π electrons of the benzene molecule and the d-band of Pd. The d-band of the Pd surface is narrow, and the interaction energy between π electrons of the benzene molecule and the d-band is ~1.19eV on the surfaces of Pd NPs, which results in strong chemisorption of C_6H_6 onto Pd NPs.

It is worth noting the higher response of Au functionalized sensors towards CO relative to the response of Pd functionalized towards C_6H_6 (with almost the same morphology). This can be attributed to higher catalytic activity of Au relative to Pd (due to the higher conductive nature and availability of more free electrons in Au) and the smaller kinetic diameter of CO (3.76Å) relative to C_6H_6 (5.85Å). Therefore, CO gas can diffuse deeper into the sensor and a higher response can be observed [55,56].

Table 1 [11,12,57–75] compares the sensing results of the present study with those of other rGO-based gas sensors. Most rGO sensors have good NO_2 sensing capability, and few studies were focused on the sensing of reducing gases by rGO-based gas sensors. As shown, the response of the present sensors is significantly higher than those reported for other gas sensors, demonstrating their good potential for practical applications.

Some groups reported the detection of a particular gas in gas mixtures because mixtures would be used in real applications, where a mixture of interfering gases exist in the atmosphere. For example, Moreira et al. [76], reported the selective detection of H_2 in a mixture of H_2, CH_4 and CO gases. Viricelle et al. [77] reported the selective detection of CO in a mixture of CO+C_3H_8 gases. Also, Akyiama et al. [78] reported the detection of acetone and benzene using selenium nanowires sensor. In the present study, we did not perform sensing experiments in a mixture of interfering gases. But, this aspect will be tested in the future, where we will try to selectively detect CO or C_6H_6 gases in a mixture of gases like CO+CO_2+ hydrocarbons (CH_x) gases or other similar gas mixtures.

4. Conclusions

Au or Pd-functionalized rGO-loaded ZnO NFs were prepared by a combination of simple and cost-effective sol-gel and electrospinning methods. The synthesized products were characterized by different techniques (FE-SEM, TEM, XRD and XPS). The large surface area and special characteristics of these ternary composites inspired us to test their response to various toxic gases. Very low concentrations of CO, C_6H_6, and C_7H_8 gases were chosen and tested. The sensing results showed that the Au-functionalized sensors were quite sensitive to CO, whereas the Pd-functionalized sensors showed a higher sensitivity to C_6H_6. Apart from the catalytic effects of Au and Pd NPs, the hybrid sensing mechanism, which combines the effects of radial resistance modulation, ZnO/ZnO grain boundary modulation, and local heterojunctions due to the presence of rGO, were the main reasons for the enhanced sensitivity of Au or Pd-functionalized rGO-loaded ZnO NFs.

Acknowledgments

This research was supported by Basic Science Research Program through the National Research Foundation of Korea (NRF) funded by the Ministry of Education (No. 2016R1D1A1B03935228).

References

[1] C.N.R. Rao, A.K. Sood, K.S. Subrahmanyam, A. Govindaraj, Graphene: the newtwo-dimensional nanomaterial, Angew. Chem. Int. Ed. 48 (2009) 7752–7777.
[2] C. Lee, X. Wei, J.W. Kysar, J. Hone, Measurement of the elastic properties andintrinsic strength of monolayer graphene, Science 321 (2008) 385–388.
[3] T.V. Tam, S.H. Hur, J.S. Chung, W.M. Choi, Ultraviolet light sensor based on graphene quantum dots/reduced graphene oxide hybrid film, Sens. Actuators A 233 (2015) 368–373.
[4] W. Yuan, G. Shi, Graphene-based gas sensors, J. Mater. Chem. A 1 (2013) 10078–10091.
[5] Y.Xu Ji, W. Zhang, L. Cui, J. Liu, Review of functionalization, structure and properties of graphene/polymer composite fibers, Composites: Part A 87 (2016) 29–45.
[6] S. Mutyala, J. Mathiyarasu, A reagentless non-enzymatic hydrogen peroxide sensor presented using electrochemically reduced graphene oxide modified glassy carbon electrode, Mater. Sci. Eng. C 69 (2016) 398–406.
[7] H. Nguyen, C. Lamiel, D. Kharismadewi, V.C. Tran, J.J. Shim, Covalently bonded reduced graphene oxide/polyaniline composite for electrochemical sensors and capacitors, J. Electroanal. Chem. 758 (2015) 148–155.
[8] D. Chen, J. Jiang, X. Du, Electrocatalytic oxidation of nitrite using metal-free nitrogen-doped reduced graphene oxide nanosheets for sensitive detection, Talanta 155 (2016) 329–335.
[9] F. Schedin, A.K. Geim, S.V. Morozov, E.W. Hill, P. Blake, M.I. Katsnelson, K.S. Novoselov, Detection of individual gas molecules adsorbed on graphene, Nat. Mater. 6 (2007) 652–655.
[10] S.G. Chatterjee, S.C. Chatterjee, A.K. Ray, A.K. Chakraborty, Graphene-metal oxide nanohybrids for toxic gas sensor: a review, Sens. Actuators B 221 (2015) 1170–1181.
[11] Y. Xiao, Q. Yang, Z. Wang, R. Zhang, Y. Gao, P. Sun, Y. Sun, G. Lu, Improvement of NO_2 gas sensing performance based on discoid tin oxide modified by reduced graphene oxide, Sens. Actuators B 227 (2016) 419–426.
[12] S. Liu, B. Yu, H. Zhang, T. Fei, T. Zhang, Enhancing NO_2 gas sensing performances at room temperature based on reduced graphene oxide-ZnO nanoparticles hybrids, Sens. Actuators B 202 (2014) 272–278.
[13] K. Anand, O. Singh, M.P. Singh, J. Kaur, R.C. Singh, Hydrogen sensor based on graphene/ZnO nanocomposite, Sens. Actuators, B 195 (2014) 409–415.
[14] G. Lu, L.E. Ocola, J. Chen, Gas detection using low-temperature reduced graphene oxide sheets, Appl. Phys. Lett. 94 (8) (2009) 083111.
[15] R. Kumar, O. Al-Dossary, G. Kumar, A. Umar, Zinc oxide nanostructures for NO_2 gas-sensor applications: a review, Nano-Micro Lett. 7 (2) (2015) 97–120.
[16] A. Kołodziejczak-Radzimska, T. Jesionowski, Zinc oxide-from synthesis to application: a review, Materials 7 (4) (2014) 2833–2881.
[17] Z.U. Abideen, A. Katoch, J.H. Kim, Y.J. Kwon, H.W. Kim, S.S. Kim, Excellent gas detection of ZnO nanofibers by loading with reduced graphene oxide nanosheets, Sens. Actuators B 221 (2015) 1499–1507.
[18] J.H. Kim, P.W.H.W. Kim, S.S. Kim, Highly selective sensing of CO, C_6H_6, and C_7H_8 gases by catalytic functionalization with metal nanoparticles, ACS Appl. Mater. Interfaces 8 (2016) 7173–7183.
[19] L. Mädler, T. Sahn, G.A. urlo, J.D. Grunwaldt, N. Barsan, U. Weimar, S.E. Pratsinis, Sensing low concentrations of CO using flame-spray-made Pt/SnO_2 nanoparticles, J. Nanopart. Res. 8 (2006) 783–796.
[20] W. Zheng, X. Lu, W. Wang, Z. Li, H. Zhang, Z. Wang, X. Xu, S. Li, C. Wang, Assembly of Pt nanoparticles on electrospun In_2O_3 nanofibers for H_2S detection, J. Colloid Interface Sci. 338 (2009) 366–370.
[21] S.S. Kim, J.Y. Park, S.W. Choi, H.S. Kim, H.G. Na, J.C. Yang, H.W. Kim, Significant enhancement of the sensing characteristics of In_2O_3 nanowires by functionalization with Pt nanoparticle, Nanotechnology 21 (2010) 415502–415509.
[22] J.H. Kim, A. Katoch, H.W. Kim, S.S. Kim, Realization of ppm-level CO detection with exceptionally high sensitivity using reduced graphene oxide-loaded SnO_2 nanofibers with simultaneous Au functionalization, Chem. Commun. 52 (2016) 3832–3835.
[23] W.S. Hummers, R.E. Offeman, Preparation of graphitic oxide, J. Am. Chem. Soc. 80 (1958) 1339.
[24] J.H. Lee, A. Katoch, S.W. Choi, J.H. Kim, H.W. Kim, Sang Sub Kim, Extraordinary improvement of gas-sensing performances in SnO_2 nanofibers due to creation of local p-n heterojunctions by loading reduced graphene oxide nanosheets, ACS Appl. Mater. Interfaces 7 (2015) 3101–3109.

[25] J.M. Choi, J.H. Byun, S.S. Kim, Influence of grain size on gas-sensing properties of chemiresistivep-type NiO nanofibers, Sens. Actuators B 227 (2016) 149–156.
[26] J.H. Kim, A. Katoch, S.H. Kim, S.S. Kim, Chemiresistive sensing behavior of SnO_2 (n)-Cu_2O (p) core-shell nanowires, ACS Appl. Mater. Interfaces 221 (2015) 15351–15358.
[27] B. Han, X. Liu, X. Xing, N. Chen, X. Xiao, S. Liu, Y. Wang, A high response butanol gas sensor based on ZnO hollow spheres, Sens. Actuators, B 237 (2016) 423–430.
[28] A. Saáedi, R. Yousefi, F.J. Sheini, A.K. Zakd, M. Cheraghizade, M.R. Mahmoudiane, M.A. Baghchesaraf, A.S.I Dezakig,XPS studies and photocurrent applications of alkali-metals-doped ZnO nanoparticles under visible illumination conditions, Physica E 79 (2016) 113–118.
[29] M. Brun, A. Berthet, J.C. Bertolini, XPS, AES and auger parameter of Pd and PdO, J. Electron Spectrosc. Relat. Phenom. 104 (1999) 55–60.
[30] F. Li, S. Guo, J. Shen, L. Shen, D. Sun, B. Wang, Y. Chena, S. Ruan, Xylene gas sensor based on Au-loaded $WO_3 \cdot H_2O$ nanocubes with enhanced sensing performance, Sens. Actuators, B 238 (2017) 364–373.
[31] A.Q. Wang, J.H. Liu, S.D. Lin, T. Lin, C.Y. Mou, A novel efficient AuAg alloy catalyst system: preparation, activity, and characterization, J. Catal. 233 (2005) 186–197.
[32] S.W. Choi, A. Katoch, G.J. Sun, J.H. Kim, S.H. Kim, S.S. Kim, Dual functional sensing mechanism in SnO_2-ZnO core-shell nanowires, ACS Appl. Mater. Interfaces 6 (2014) 8281–8287.
[33] J. Rebholz, P. Bonanati, C. Jaeschke, M. Hübner, L. Mädler, U. Weimar, N. Barsan, Conduction mechanism in undoped and antimony doped SnO_2 based FSP gas sensors, Sens. Actuators B 188 (2013) 631–636.
[34] N. Bârsan, M. Hübner, U. Weimar, Conduction mechanisms in SnO_2 based polycrystalline thick film gas sensors exposed to CO and H_2 in different oxygen backgrounds, Sens. Actuators B 157 (2011) 510–517.
[35] A.P. Lee, B.J. Reedy, Temperature modulation in semiconductor gas sensing, Sens. Actuators B 60 (1999) 35–42.
[36] G. Korotcenkov, B.K. Cao, Engineering approaches for the improvement of conductometric gas sensor parameters: part 1. Improvement of sensor sensitivity and selectivity (short survey), Sens. Actuators, B 188 (2013) 709–728.
[37] M.F. Al-Kuhaili, S.M.A. Durrani, I.A. Bakhtiari, Carbon monoxide gas-sensing properties of CeO_2-ZnO thin films, Appl. Surf. Sci. 255 (2008) 3033–3039.
[38] N.D. Khoang, N.V. Duy, N.D. Ho, N.V. Hieu, Design of SnO_2/ZnO hierarchical nanostructures for enhanced ethanol gas-sensing performance, Sens. Actuators B 174 (2012) 594–601.
[39] A. Mirzaei, K. Janghorban, B. Hashemi, G. Neri, Metal-core@metal oxide-shell nanomaterials for gas-sensing applications: a review, J. Nanopart. Res. 17 (2015) 1–36.
[40] Bhagavathi Parambhath, R. Nagar, K. Sethupathi, S. Ramaprabhu, Investigation of spillover mechanism in palladium decorated hydrogen exfoliated functionalized graphene, J. Phys. Chem. C 115 (2011) 15679–15685.
[41] J.S. Lee, A. Katoch, J.H. Kim, S.S. Kim, Effect of Au nanoparticle size on the gas-sensing performance of p-CuO nanowires, Sens. Actuators B 222 (2016) 307–314.
[42] S.S. Kim, J.Y. Park, S.W. Choi, H.S. Kim, H. Gna, J.C. Yang, C. Lee, H.W. Kim, Room temperature sensing properties of networked GaN nanowire sensors to hydrogen enhanced by the Ga_2Pd_5 nanodot functionalization, Int. J. Hydrogen Energy 36 (2011) 2313–2319.
[43] W.C. Conner Jr, J.L. Falconer, Spillover in heterogeneous catalysis, Chem. Rev. 95 (1995) 759–788.
[44] M.E. Franke, T.J. Koplin, U. Simon, Metal and metal oxide nanoparticles in chemiresistors: does the nanoscale matter? Small 2 (2006) 36–50.
[45] Y. Li, J. Gong, G. He, Y. Deng, Enhancement of photoresponse and UV-assisted gas sensing with Au decorated ZnO nanofibers, Mater. Chem. Phys. 134 (2012) 1172–1178.
[46] S. Peng, Y. Lee, C. Wang, H. Yin, S. Dai, S. Sun, A facile synthesis of monodisperse Au nanoparticles and their catalysis of CO oxidation, Nano Res. 1 (3) (2008) 229–234.
[47] H.Y. Kim, H.M. Lee, G. Henkelman, CO oxidation mechanism on CeO_2-supported Au nanoparticles, J. Am. Chem. Soc. 134 (3) (2012) 1560–1570.
[48] H. Wang, S. Yin, S. Dai, Sun A general approach to noble metal–metal oxide dumbbell nanoparticles and their catalytic application for CO oxidation, Chem. Mater. 22 (10) (2010) 3277–3282.
[49] H. Fu, C. Hou, F. Gu, D. Han, Z. Wang, Facile preparation of rod-like Au/In_2O_3 nanocomposites exhibiting high response to CO at room temperature, Sens. Actuators B. Chem. 243 (2017) 516–524.
[50] M. Nishiboria, W. Shina, N. Izua, T. Itoha, I. Matsubara, CO oxidation performance of Au/Co_3O_4 catalyst on the micro gas sensor device, Catal. Today 201 (2013) 85–91.
[51] G. Mpourmpakis, A.N. Andriotis, D.G. Vlachos, Identification of descriptors for the CO interaction with metal nanoparticles, Nano Lett. 10 (2010) 1041–1045.
[52] Z. Zanolli, R. Leghrib, A. Felten, J.J. Pireaux, E. Llobet, J.C. Charlier, Gas sensing with Au-decorated carbon nanotubes, Acs Nano 5 (6) (2011) 4592–4599.
[53] J.H. Kim, H.W. Kim, S.S. Kim, Ultra-sensitive benzene detection by a novel approach: core-shell nanowires combined with the Pd-functionalization, Sens. Actuators B 239 (2017) 578–585.
[54] C. Morin, D. Simon, P. Sautet, Chemisorption of benzene on Pt (111), Pd (111), and Rh (111) metal surfaces: a structural and vibrational comparison from first principles, J. Phys. Chem. B 108 (18) (2004) 5653–5665.
[55] C.A. Scholes, S.E. Kentish, G.W. Stevens, Effects of minor components in carbon dioxide capture using polymeric gas separation membranes, Separ. Purific. Rev. 38 (1) (2009) 1–44.
[56] A.S.M.I. Uddin, D.T. Phan, G.S. Chung, Low temperature acetylene gas sensor based on Ag nanoparticles-loaded ZnO-reduced graphene oxide hybrid, Sens. Actuators B 207 (2015) 362–369.
[57] P.G. Su, L.Y. Yang, NH_3 gas sensor based on Pd/SnO_2/RGO ternary composite operated at room-temperature, Sens. Actuators B 223 (2016) 202–208.
[58] A.Irajizad Esfandiar, O. Akhavan, S. Ghasemi, M.R. Gholami, Pd-WO_3/reduced graphene oxide hierarchical nanostructures as efficient hydrogen gas sensors, Int. J. Hydrogen Energy 39 (2014) 8169–8179.
[59] X. Lia, J. Wang, D. Xie, J. Xu, R. Dai, L. Xiang, H. Zhuc, Y. Jiange, Reduced graphene oxide/hierarchical flower-like zinc oxide hybrid films for room temperature formaldehyde detection, Sens. Actuators B 221 (2015) 1290–1298.
[60] Q. Feng, X. Li, J. Wang, A.M. Gaskov, Reduced graphene oxide (rGO) encapsulated Co_3O_4 composite nanofibers for highly selective ammonia sensors, Sens. Actuators B 222 (2016) 864–870.
[61] M. MalekAlaie, M. Jahangiri, A.M. Rashidi, A. HaghighiAsl, N. Izadi, Selective hydrogen sulfide (H_2S) sensors based on molybdenum trioxide (MoO_3) nanoparticle decorated reduced graphene oxide, Mater. Sci. Semicond. Process. 38 (2015) 93–100.
[62] U. Yaghob, A.S.M. Udin, G.S. Chung, A high-performance flexible NO_2 sensor based on WO_3 NPs decoratedon MWCNTs and RGO hybrids on PI/PET substrates, Sens. Actuators B 224 (2016) 738–746.
[63] Y. Zhou, Y. Jiang, T. Xie, H. Tai, G. Xie, A novel sensing mechanism for resistive gas sensors based on layeredreduced graphene oxide thin films at room temperature, Sens. Actuators B 203 (2014) 135–142.
[64] W.Y. Yan, Q. Zhang, X. Chen, X.J. Huang, Y.C. Wua, C-doped and N-doped reduced graphene oxide/TiO_2 composites withexposed (001) and (101) facets controllably synthesized by ahydrothermal route and their gas sensing characteristics, Sens. Actuators B 230 (2016) 761–772.
[65] S. Deng, V. Tjoa, H.M. Fan, H.R. Tan, D.C. Sayle, M. Olivo, S. Mhaisalkar, J. Wei, C.H. Sow, Reduced graphene oxide conjugated Cu_2O nanowire mesocrystals for high-performance NO_2 gas sensor, J. Am. Ceramic Soc. 134 (2012) 4905–4917.
[66] J. Qin, M. Cao, N. Li, C. Hu, Graphene-wrapped WO_3 nanoparticles with improved performances in electrical conductivity and gas sensing properties, J. Mater. Chem. 21 (2011) 17167–17171.
[67] S. Srivastava, K.J.V.N. Singh, S. Singh, N. Vijayan, N. Dilawar, G. Gupta, T.D. Senguttuvan, Faster response of NO_2 sensing ingrapheme-WO_3 nanocomposites, Nanotechnology 23 (2012) 205501.
[68] L.T. Hoa, H.N. Tien, V.H. Luan, J.S. Chung, S.H. Hur, Fabrication of a novel 2D-graphene/2D-NiO nanosheet-based hybrid nanostructure and its use in highly sensitive NO_2 sensors, Sens. Actuators B 185 (2013) 701–705.
[69] N. Chen, X. Li, X. Wang, J. Yu, J. Wang, Z. Tang, S.A. Akbar, Enhanced room temperature sensing of Co_3O_4-intercalated reduced graphene oxide based gas sensors, Sens. Actuators B: Chem. 188 (2013) 902–908.
[70] P.G. Su, S.L. Peng, Fabrication and NO_2 gas-sensing properties of reduced graphene oxide/WO_3 nanocomposite films, Talanta 132 (2015) 398–405.
[71] C.Y. An, Y. Jimmy, Y.Hu Wang, X.Yu G.Zhang, WO_3 nanorods/graphene nanocomposites for high-efficiency visible-light-driven photocatalysis and NO_2 gas sensing, J. Mat. Chem. 22 (2012) 8525–8531.
[72] C. Balamurugan, S. Arunkumar, D.W. Lee, Hierarchical 3D nanostructure of $GdInO_3$ and reduced-graphene-decorated $GdInO_3$ nanocomposite for CO sensing applications, Sens. Actuators B 234 (2016) 155–166.
[73] S.F. Bamsaoud, S.B.R.R.N. Karekar, R.C. Aiyer, Nano particulate SnO_2 based resistive films as a hydrogen and acetone vapour sensor, Sens. Actuators B 153 (2011) 382–391.
[74] C. Feng, X. Li, J. Ma, Y. Sun, C. Wang, P. Sun, J. Zheng, G. Lu, Facile synthesis and gassensing properties of In_2O_3-WO_3 heterojunction nanofibers, Sens. Actuators B 209 (2015) 622–629.
[75] Q. Vu Van, N.V. Dung, T. Ngo Sy, H. Nguyen Duc, D. Nguyen Van, H. Nguyen Van, Outstanding gas-sensing performance of graphene/SnO_2 nanowire Schottky junctions, Appl. Phys. Lett. 105 (2014) 013107.
[76] R.G. Moreira, L.H. Moreira, S.G. dosSantosFilho, Sensing different mixtures of H_2, CH_4 and CO through an array of chemiresistors, Microelectronics Technology and Devices (SBMicro), 2014, 29th Symposium on IEEE (2017) 1–4.
[77] J.P. Viricelle, A. Valleron, C. Pijolat, P. Breuil, S. Ott, Gas sensors based on tin dioxide for exhaust gas application: modeling of response for pure gases and for mixtures, Procedia Eng. 47 (2012) 655–658.
[78] N. Akiyama, A sensor array based on trigonal-selenium nanowires for the detection of gas mixtures, Sens. Actuators, B 223 (2016) 131–137.

Biographies

Zain Ul Abideen received his B.S. in Materials Engineering from Ghulam Ishaq Khan Institute of Engineering Sciences and Technology (GIK Institute), Pakistan in June 2014. In February 2016, he received M.S. degree from Inha University, Republic of Korea under the supervision of Professor Sang Sub Kim. He is currently working for a company as a researcher in Republic of Korea.

Jae-Hun Kim received his B.S. degree from Gyeongsang National University, Republic of Korea in 2013. In February 2015, he received M.S. degree from Inha University, Republic of Korea. He is now working as a Ph.D. candidate at Inha University, Republic of Korea. He has been working on oxide nanowire gas sensors.

Ali Mirzaei received his Ph.D. degree in Materials Science and Engineering from Shiraz University in 2016. He was a visiting student at Messina University, Italy in 2015. Since 2016 he is a postdoctoral fellow at Hanyang University in Seoul. He is interested in the synthesis and characterization of nanocomposites for gas sensing applications.

Hyoun Woo Kim joined the Division of Materials Science and Engineering at Hanyang University as a full professor in 2011. He received his B.S. and M. S. degrees from Seoul National University and his Ph.D. degree from Massachusetts Instituteof Technology (MIT) in electronic materials in 1986, 1988, and 1994, respectively. He was a senior researcher in the Samsung Electronics Co., Ltd. from 1994 to 2000. He has been a professor of materials science and engineering at Inha University from 2000 to 2010. He was a visiting professor at the Department of Chemistry of the Michigan State University in 2009. His research interests include the one-dimensional nanostructures, nanosheets, and gas sensors.

Sang Sub Kim joined the Department of Materials Science and Engineering, Inha University, in 2007 as a full professor. He received his B.S. degree from Seoul National University and his M.S and Ph.D. degrees from Pohang University of Science and Technology (POSTECH) in Material Science and Engineering in 1987, 1990, and 1994, respectively. He was a visiting researcher at the National Research in Inorganic Materials (currently NIMS), Japan for 2 years each in 1995 and in 2000. In 2006, he was a visiting professor at Department of Chemistry, University of Alberta, Canada. In 2010, he also served as a cooperative professor at Nagaoka University of Technology, Japan. His research interests include the synthesis and applications of nanomaterials such as nanowires and nanofibers, functional thin films, and surface and interfacial characterizations.